



Paleoceanography and Paleoclimatology

RESEARCH ARTICLE

10.1029/2017PA003293

Key Points:

- Here we present a new tool for paleoclimate time series research
- This technique is based on the concept of spectral moments
- Spectral moments in this study are descriptive quantities of the periodogram, evaluated over all the frequencies in the Nyquist band

Supporting Information:

- Supporting Information S1
- Data Set S1

Correspondence to:

M. Sinnesael,
matthias.sinnesael@vub.be

Citation:

Sinnesael, M., Zivanovic, M., De Vleeschouwer, D., & Claeys, P. (2018). Spectral moments in cyclostratigraphy: Advantages and disadvantages compared to more classic approaches. *Paleoceanography and Paleoclimatology*, 33, 493–510. <https://doi.org/10.1029/2017PA003293>

Received 20 NOV 2017

Accepted 22 APR 2018

Accepted article online 7 MAY 2018

Published online 19 MAY 2018

Spectral Moments in Cyclostratigraphy: Advantages and Disadvantages Compared to More Classic Approaches

Matthias Sinnesael¹ , Miroslav Zivanovic², David De Vleeschouwer^{1,3} , and Philippe Claeys¹

¹AMGC - Analytical, Environmental, and Geochemistry, Vrije Universiteit Brussel, Brussels, Belgium, ²Department of Electrical and Electronic Engineering, Universidad Pública de Navarra, Pamplona, Spain, ³MARUM - Center for Marine Environmental Science, University of Bremen, Bremen, Germany

Abstract Cyclostratigraphic analyses rely on techniques that trace astronomical components in paleoclimate signals. These techniques have demonstrated their value but rely on certain assumptions on the presence and quality of the astronomical imprint. Here we explore a new conceptual approach to time series analysis. Specifically, we evaluate the potential of spectral moments to characterize the full spectral characteristics of a record and thus not only the frequency ranges of interpreted astronomical components. Mathematically speaking, moments are unique quantities describing a specific set of points. In the case of spectral moments, we apply the concept of moments on the distribution of spectral power in a signal's periodogram. We present four case studies that illustrate the advantages and disadvantages of the spectral moment approach in gaining insight in the (astronomical) features of a particular data record. We discuss the effects of outliers in a series, variable sedimentation rate, and changing climate dynamics on the spectral moments of a power spectrum. At the same time, we carry out a sedimentation rate reconstruction based on the spectral moment approach and compare that reconstruction to results obtained through classic approaches. Compared to classic approaches, the spectral moments approach is robust and requires less strict assumptions to obtain similar first-order information. Yet such assumptions are still necessary to achieve more precise sedimentation rate reconstructions. In summary, we show that the spectral moments approach is suitable to obtain first-order insights in variable components embedded in a depth series.

1. Introduction

Since the 1970s of the twentieth century, there has been a revived interest in the astronomical theory as a major forcing of the paleoclimate system (Berger, 1978; Hays et al., 1976; Imbrie, 1982). In parallel, cyclostratigraphy and astrochronology became indispensable tools for the field of stratigraphy (Hinnov, 2013; Hinnov & Hilgen, 2012). Cyclostratigraphic studies can be carried out in various manners, often based on spectral analysis or wavelet techniques (e.g., Meyers et al., 2001; Muller & MacDonald, 2000; Thomson, 1982; Torrence & Campo, 1998). The existing approaches aim at the identification and tracking of one or several astronomical components and commonly do not treat the full spectral characteristics of the record. The classic time series analysis techniques are useful and powerful tools but often rely on one or more of the following assumptions: the (same) orbital components are present throughout a record, the signal-to-noise ratio is sufficient to detect an astronomical imprint, and there are not too strong variations in sedimentation rate or other disturbing factors (e.g., hiatuses). When these assumptions are not valid, one moves from an estimation (of the astronomical components) toward a detection problem. The (evolutive) average spectral misfit method considers several astronomical components from the same spectrum in a single analysis (Meyers et al., 2012; Meyers & Sageman, 2007). Using this technique, Meyers and Sageman (2007) illustrated the contraction and expansion of a given spectrum for different sedimentation rates. When sedimentation rate increases, the astronomical components in a depth-domain spectrum shift to lower frequencies, and vice versa. Nonetheless, the ratios between astronomically forced peaks in the spectrum are maintained (Figure 1 in Meyers and Sageman, 2007). This method is however still based on the identification of significant and individual components of a spectrum.

In this work, we examine the possibility to use the full spectral characteristics of a record, by the application of spectral moments, in a geologic and cyclostratigraphic context. Mathematically speaking, moments are unique quantities describing a specific set of points. For example in mechanics, the moments can describe the distribution of mass in a system. In statistics, the set of points can represent probability densities. For

instance, for the commonly used normal distribution one would characterize its distribution by the mean (first moment), the variance (second moment), and so on. In this study, we apply the concept of moments to a power spectrum, therewith describing the spectral distribution of a signal, to explore the advantages and disadvantages of such approach in a cyclostratigraphic context. Indeed, there is currently no classic cyclostratigraphic tool that uses spectral moments to quantify the imprint of astronomical forcing in a geologic archive. The motivation for this research arises from several theoretical characteristics of spectral moments that could be translated into concrete geologic attributes. As mentioned before, changing sedimentation rates make a spectrum contract and expand, which will change the spectral moments. In a similar way, the occurrence of “irregularities” in an analyzed proxy record (e.g., hiatuses, sudden jumps, or anomalous values) changes the record’s spectrum and its spectral moments. One can thus conclude that changes in the spectral moments of a signal can reflect changes in geologic boundary conditions.

The goal of this study is to evaluate the merits and drawbacks of spectral moments in cyclostratigraphic applications. In section 2 of this work, we provide the theoretical background and principles of spectral moments, the technical implementation, interferences with noise, and their connection to sedimentation rates in the case of paleoclimate depth series. In the results section, we apply spectral moments to four different case studies, so to illustrate key aspects in a cyclostratigraphic context. The first case study consists of an artificially altered insolation signal to make the reader acquainted with the new concepts of spectral moments. The second case study investigates a Pleistocene Natural Gamma Ray (NGR) record from International Ocean Drilling Program (IODP) Site U1437, illustrating the effect of the presence of volcanic ash layers in the analysis of the NGR-derived K (wt %) record. The third and fourth case studies examine Pliocene and Pleistocene benthic oxygen isotope records from, respectively, Ocean Drilling Program (ODP) Sites 982 and 677 and deal with changing rates in sedimentation and global paleoclimate features.

2. Methodology: Spectral Moments

2.1. Background

Let us consider an insolation signal $h(t)$, sampled uniformly at times t_n , $n = 1 \dots N$, represented analytically as a linear combination of P sinusoids:

$$h(t_n) = \sum_{j=1}^P A_j \cos(2\pi F_j t_n + \phi_j) \quad (1)$$

with A_j for amplitude and ϕ_j for the phase and where F_j is the precession, obliquity, and eccentricity frequencies over a given time interval. Sedimentary archives record changes in climatic systems that are caused by changes in insolation as an astronomical imprint. Paleoclimate scientists usually sample such an archive at equally spaced intervals (z_n), with z_0 being the sampling interval. By doing so, they generate a sedimentary paleoclimate record $s(z_n)$. For the sake of simplicity, we here consider a linear response to the climate system to the insolation forcing, such that the sedimentary record $s(z_n)$ is related to the forcing signal by

$$s(z_n) = h(z_0 \sum_{i=1}^n r(z_i))^{-1} = \sum_{j=1}^P a_j(z_n) \cos(2\pi F_j(r(z_n))^{-1} z_n + \phi_j) \quad (2)$$

with $r(z_n)$ for sedimentation rate and a_j for amplitude. In the last expression (equation (2)) the transfer function between the time and depth domain is characterized by two factors. First, there is the depth-varying sedimentation rate $r(z_n)$. So also the astronomical components F_j are depth varying with sedimentation rate. Second, the amplitude change (a_j) in the individual frequency components in equation (2) accounts for changes in the insolation signal (equation (1)) by the response of the climatic system that may occur at different spatial frequencies and as such change A_j from equation (1).

The sedimentation rate $r(z_n)$ acts as a simultaneous inverse scaling of the P frequency components in the depth domain. In other words, the larger $r(z_n)$ the more expanded astronomical cycles will be in the depth domain and vice versa. In signal theory, this is equivalent to waveform expansion (or compression). As a result of the Fourier transform duality property, the corresponding baseband periodogram—comprehended between zero and the Nyquist spatial frequency—undergoes a compression (or expansion).

In practice, sedimentation rate rarely changes in a uniform way. Moreover, the response of the climatic system can change the amplitude ratio among the astronomical components of the original insolation forcing signal.

Accordingly, the global periodogram (calculated over the full data record) is not a sufficiently complete representation of the climatic system response and sedimentation rate dynamics along the depth scale. Instead, the data in this study are processed on a short-frame basis that yields a series of local periodograms associated to different depths. In what follows it will be shown that local periodograms can be described in a condensed manner by spectral moments, from which we can infer the dynamics of the underlying processes in geological data.

2.2. Periodogram as a Distribution

To address the present issue, a few concepts will be illustrated intuitively in the following subsection using the theory of body mechanics from physics. Further on, the aforementioned concepts are extended to the use of the periodogram of geological data.

2.2.1. Mass Distribution and Its Moments

Assume a set of M particles, located on a linear axis at the points x_i with corresponding masses $m_i(x_i)$, $i = 1 \dots M$. For such a scenario, we first define the mass distribution $p(x_i)$ as a function of normalized weights:

$$p(x_i) = \frac{m(x_i)}{\sum_{i=1}^M m(x_i)}, \quad (3)$$

$$\sum_{i=1}^M p(x_i) = 1. \quad (4)$$

The mass distribution $p(x_i)$ can also be identified as a mass density in distance. On the basis of equations (3) and (4) we define the first moment of x_i (x_i), that is, the center of mass μ_x :

$$\mu_x = \sum_{i=1}^M x_i p(x_i). \quad (5)$$

The concept of the center of mass is that of an average of the masses factored by their distances from a reference point, that is, the set of particles that respond to external forces as if the total mass was concentrated at this point. In addition to the center of mass we can calculate the second moment σ_x^2 as an average squared distance to the center of mass:

$$\sigma_x^2 = \sum_{i=1}^M (x_i - \mu_x)^2 p(x_i). \quad (6)$$

This moment, also known as the moment of inertia of the mass distribution about μ_x , quantifies the dispersion of the data with respect to center of mass of the data. The center of mass and moment of inertia are thus mathematical descriptors that allow for characterizing a possibly complicated mass distribution scenario by only two values. In addition, observe that the present discussion can be mapped onto a probabilistic context, where the moments μ_x and σ_x^2 are immediately interpreted as the standard statistical mean and variance of the data belonging to the probability density function $p(x_i)$. An important difference to keep in mind is that the spectral moments of the mass distribution (and the following applications in the rest of the paper) are however deterministic and not probabilistic in nature.

2.2.2. Periodogram and Spectral Moments

The periodogram of a data series from a sedimentary record $s(z_n)$ is defined as a squared modulus of the Discrete Fourier Transform (DFT) of the data evaluated at K spatial frequencies f_k . The periodogram represents the energy density in the frequency domain—the energy distribution. By analogy to equations (3) and (4)

$$S(f_k) = \frac{|\text{DFT}\{s(z_n)\}|^2}{\sum_{k=1}^K |\text{DFT}\{s(z_n)\}|^2} \quad (7)$$

$$\sum_{k=1}^K S(f_k) = 1, \quad k = 1 \dots K, \quad (8)$$

with $S(f_k)$ being the normalized periodogram. Further, we can define the first two moments of the normalized periodogram (equation (7)) in a way similar to equations (5) and (6) and

$$\mu_f = \sum_{k=1}^K f_k S(f_k) \quad (9)$$

$$B^2 = \sigma_f^2 = \sum_{k=1}^K (f_k - \mu_f)^2 S(f_k). \quad (10)$$

Expressions (9) and (10) represent the first two spectral moments of the periodogram, namely, the mean frequency (μ) and squared bandwidth (B^2 ; Cohen, 1995). When a short-frame analysis is performed of the geological data, then $S(f_k)$ is a normalized local periodogram and its spectral moments give a rough idea of the principal characteristics—the mean and spread—of the spectral density for the analysis frame duration. The normalization is done to remove potential energy effects caused by the framing, that is, neutralizing the effect that frames with more energy will yield larger moments than frames with less energy.

2.3. Amplitude and Phase Contribution to the Spectral Moments

It is known from the time-frequency (TF) signal analysis theory that the periodogram is shaped by a combined action of amplitude modulation (AM) and phase modulation (PM) of the underlying signal (Cohen, 1995). In the context of the present work, it will be shown that the PM is physically related to the sedimentation rate while AM explains the response of the climatic system at different frequencies in the depth domain.

It has been shown, however, that the issue of finding individual AM and PM contributions (also known as the AM-PM decomposition) is problematic because there is an infinite number of combinations of AM-PM that can generate a given multicomponent signal (Boashash, 1992). Some authors proved that under a number of constraints, there is a unique AM-PM decomposition for a multicomponent nonstationary signal (Betser et al., 2008; Gazor & RashidiFar, 2006; Loughlin & Tacer, 1996; Pantazis et al., 2011; Quatieri et al., 1997). However, the corresponding results are not applicable in an analysis scenario of an arbitrary geological signal. Nevertheless, we will illustrate that an approximate solution is achievable by taking into account the potential (astronomical) driving mechanisms behind the generation of geological signals.

2.3.1. Phase Contribution

The phase contribution is mainly coupled to the sedimentation rate $r(z_n)$, as indicated by equation (2). Assuming that $r(z_n) = r_0 = \text{Constant}$ and there is no significant change in the instantaneous amplitudes in the frequency components, the following expressions are valid:

$$s(z_n) \xrightarrow{\text{DFT}} S(f_k), \mu_f, B \quad (11)$$

$$s(r_0 t_n) \xrightarrow{\text{DFT}} \frac{1}{r_0} S\left(\frac{f_k}{r_0}\right), \frac{\mu_f}{r_0}, \frac{B}{r_0} \quad (12)$$

Meaning that the discrete depth sedimentary record $s(z_n)$ is represented in the discrete spatial frequency domain by its periodogram $S(f_k)$ and its associated spectral moments. It turns out that r_0 is exactly equal to the compression/expansion index of the given scenario, that is, the mapping between the time and spatial frequency domain is a linear one. The spectral moments are scaled by r_0 . For an arbitrary nonconstant sedimentation rate change in the short analysis frame (e.g., linear), the analytical relation between the input data and its periodogram compression/expansion is nonlinear. Still, it can be proven that equations (11) and (12) approximately hold if the rate of change (the slope of the sedimentation rate) is small compared to the frame length.

2.3.2. Amplitude Contribution

The amplitude contribution is difficult to quantify because of the nonadditivity of individual components in the periodogram. To get a deeper insight, consider the signal (equation (2)), composed of P sinusoids $s_j(z_n)$, which we rewrite in a simplified form:

$$s(z_n) = \sum_{j=1}^P s_j(z_n). \quad (13)$$

The spectrum of the signal is a sum of individual spectra; this is, unfortunately, not the case for the periodogram. By calculating the squared magnitude spectrum of (13), after some algebraic manipulations (Appendix A), we obtain

$$S(f_k) = \sum_{j=1}^P S_j(f_k) + \sum_{j=1}^P \sum_{i \neq j} S_{ij}(f_k) \neq \sum_{j=1}^P S_j(f_k) \quad (14)$$

with cross terms

$$S_{ij}(f_k) = 2\Re\{\text{DFT}(s_j(z_n))^* \text{DFT}(s_i(z_n))\}, \quad (15)$$

where the symbol “*” stands for the complex conjugate operator while “ R ” represents the real part of a complex value. As obvious from equation (14), the periodogram of the input signal is a sum of individual periodograms plus the cross terms ($S_{ij}(f_k)$) that account for all possible cross spectra among the individual sinusoids in the signal. The physical reason behind equations (14) and (15) is that when a number of sinusoids with arbitrary nominal frequencies add up, the waveforms may add and interfere in different ways, thus changing the weights of individual components. This phenomenon becomes even stronger for a short analysis frame because the windowing effect makes the intercomponent interference stronger. Windowing makes individual components in the frequency domain stretch. As a result, overlap among those components increases and the interference between the components as well. The shorter the window is, the larger the interference will be. Consequently, it is to be expected that the presence of cross terms will affect the spectral moments. Combining equations (9) and (10) with equations (14) and (15) we can obtain the following generic expressions for the spectral moments:

$$\mu_f = \sum_{j=1}^P \mu_f(j) + \sum_{j=1}^P \sum_{i \neq j} \mu_f(i, j), \quad (16)$$

$$B^2 = \sum_{j=1}^P B^2(j) + \sum_{j=1}^P \sum_{i \neq j} B^2(i, j), \quad (17)$$

with the index j still standing for 1 to P sinusoidal (orbital) components in the signal, while index i (1 to P) is different to j to obtain the cross terms. The last expressions should be interpreted in the following way. A spectral moment of the local periodogram, that is, the periodogram of an analysis frame, is a sum of individual and cross-component moments. An individual spectral moment for a given sinusoidal component represent the dynamics of its periodogram solely. A cross-component spectral moment of two sinusoidal components characterizes the corresponding cross periodogram.

So, what does this mean in the context of a frame-based analysis of a geological signal? The individual spectral moments (the first sum in equations (16) and (17)) stay constant for the whole duration of the input data, because the energy distribution of a sinusoidal component does not change over the depth. The cross-component spectral moments (double sums in equations (16) and (17)) do change from frame to frame because the sinusoidal phases are different in each frame. Therefore, the amplitude contribution to the spectral moments of a geological series with constant sedimentation rate is twofold: a constant terms plus fast varying terms. How fast the latter vary will depend on the depth lag between the contiguous analysis frames. The depth lag between the contiguous frames is the step we move the frame along the record; for a smaller time step the output gets smoother and the other way around.

2.3.3. Spectral Moments and Noise

Sedimentary archives record astronomically driven environmental change in a nonlinear manner. First of all, the forcing signal is distorted along its propagation through the climate and depositional systems (e.g., discussions in Meyers et al., 2008 and Li et al., 2018). Second, different sources of noise complicate the interpretations of proxy measurements. Some of the perturbation sources are well studied, and the corresponding modeling and analysis frameworks are in use (e.g., red noise process related to the climate system dynamics; Meyers, 2012). Other phenomena, for example, diagenesis, can comprehend a complex series of processes that are seldom described in a general analytical manner. Accordingly, it is a difficult task to take into account all possible disturbances. Whatever a real signal might be, we assume that within the analysis frame the noise is homogeneous. Assuming that the mechanism through which the noise affects the spectral moments does not change, average noise properties (e.g., variance change over depth), will only put more or less bias on the spectral moments along the depth axis. Indeed this does not take into account all imaginable noise variations along the record—which is extremely difficult and explains also why other studies have assumed similar stationary white noise behavior over a record. Nevertheless, for assessment of the algorithm performance in noisy environments we can still identify main perturbation sources along the pathway of the orbital signal and provide a rough analysis of noise impact onto the spectral moments.

A block diagram in Figure 1 shows a conceptual model of approximate locations of the principal noise sources along the insolation signal pathway in the signal processing domain. Red noise is typically a low-frequency random signal that arises by power spectrum shaping of the white noise by some slow-response climate-related system (e.g., Mann & Lees, 1996). In the conceptual model of this study, red noise is added to the (insolation) signal at the initial processing stage, which roughly corresponds to the primary response of

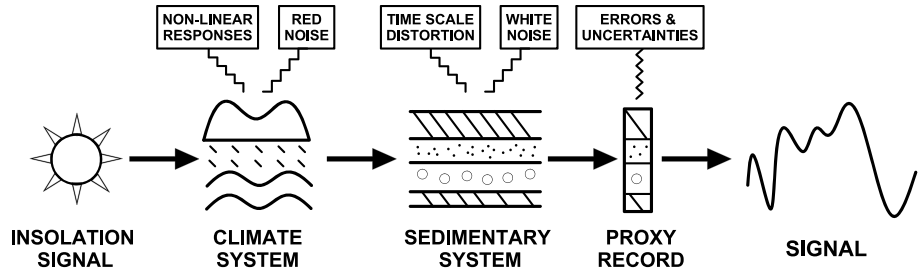


Figure 1. Principal noise sources along the orbital-insolation signal pathway.

the climate system. Subsequently, the altered signal (insolation with red noise) undergoes a time scale distortion as a result of the response of the depositional and sedimentary system. This distortion is provoked by a variable accumulation rate. The resulting signal can be further perturbed by other sources of white noise like sampling effects and analytical errors. The white noise spreads uniformly over the whole baseband, that is, from zero to the Nyquist frequency $f_s/2$, where f_s is the sampling rate. Note that this scheme does not include all possible distortions and sources of noise, as well as possible feedbacks with the climate.

According to Figure 1 and equations (11) and (12) we can express the spectrogram of the measurements in the analysis frame centered at an arbitrary depth z_n :

$$S(f_k, z_n) = S_{0r}(f_k, r(z_n)) + S_w(f_k, z_n), \quad (18)$$

where S_{0r} represents the joint spectrogram of the orbital signal and red noise, while S_w stands for the periodogram of the white noise. Note that the former is also a function of the sedimentation rate imposed by the depositional system. Let us assume that the red noise correlation coefficient is moderate/large, that is, most energy of the red noise is clustered in a frequency band around the orbital components. Accordingly, S_{0r} behaves as a low pass that means that most of its energy (e.g., 95%) falls in the frequency range $[0, f_c]$, where f_c is known as a cutoff frequency (recall that the signal energy is equal to the area under the periodogram). So the value of the cutoff frequency f_c will depend for each periodogram in each analysis frame on its distribution. The complementary frequency range, which is defined as the interval between the cutoff frequency f_c and the Nyquist frequency $f_s/2$, contains mostly white noise, and therefore,

$$S(f_k, z_n) \approx \begin{cases} S_{0r}(f_k, r(z_n)), & 0 \leq f_k < f_c(r(z_n)) \\ S_w(f_k, z_n), & f_c(r(z_n)) \leq f_k < f_s/2 \end{cases} \quad (19)$$

Note in equation (19) that f_c is a function of a depth-varying sedimentation rate. By combining equation (18) with equations (9) and (10) and dropping z_n for the sake of clearness, we get the following generic expressions for the spectral moments:

$$\mu_f \approx \sum_{k=1}^{c-1} f_k S_{0r}(f_k, r) + \sum_{k=c}^N f_k S_w(f_k) = \mu_{f,0r} + \mu_{f,w} \quad (20)$$

$$B^2 \approx \sum_{k=1}^{c-1} (f_k - \mu_f)^2 S_{0r}(f_k, r) + \sum_{k=c}^N (f_k - \mu_f)^2 S_w(f_k) = B_{0r}^2 + B_w^2 \quad (21)$$

with $c = c(r(z_n))$ being the DFT sample index corresponding to the sedimentation rate dependent cutoff frequency.

According to the last expressions, the first term in the spectral moments is determined by a composite spectrogram of the analyzed signal plus red noise with a modified time scale by the sedimentation rate. This spectrogram expands/compresses opposite to the sedimentation rate— $\mu_{f,0r}$ and B_{0r}^2 —and approximately follows the phase change in the (potential) orbital components. In addition, the periodogram cross terms will generate additional fast variations around the trend in the spectral moments. The size and distribution of those variations will be random in nature and determined by the correlation between the orbital and red noise components.

The second term in equations (20) and (21) is determined by a uniformly distributed white noise power along a variable frequency range approximately equal to $(f_s/2 - f_c)$. Observe that this range fluctuates with f_c .

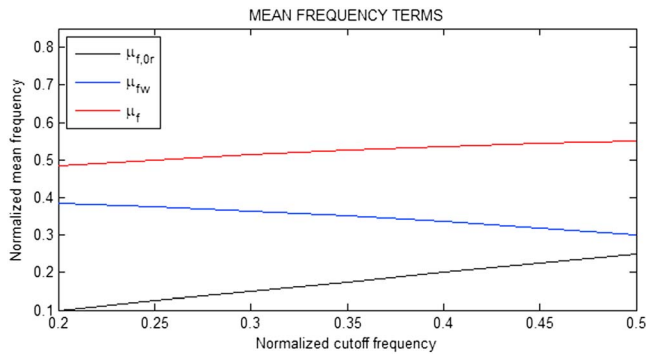


Figure 2. Mean frequency terms against the cutoff frequency (the normalization is with respect to the Nyquist frequency).

therefore, the noise contribution to the mean frequency will implicitly be a function of the sedimentation rate. This contribution can be expressed analytically as follows. Assuming that $\mu_{f,0r} = f_c/2$; then, it can be shown (see Appendix B) that the mean frequency μ_f can be written as

$$\mu_f = \mu_{f,0r} + \mu_{f,w} = \frac{f_s}{4N} [c + \overline{S_w}(N^2 - c(c+1))] \quad (22)$$

with $\overline{S_w} = \sigma_w^2/f_s$ and σ_w^2 being the white noise variance. Note that while $\mu_{f,0r}$ varies linearly, $\mu_{f,w}$ changes quadratically in the opposite direction. As a result, $\mu_{f,w}$ is a bias that acts as a trend smoother in $\mu_{f,0r}$. For example, if the sedimentation rate decreases over depth, $\mu_{f,0r}$ increases while $\mu_{f,w}$ decreases and thus “pulls down” μ_f . To get a deeper insight, the mean frequency terms in equation (22) are plotted in Figure 2 against the normalized cutoff frequency. In this case we let $N = 1000$, $f_s = 50$ samples/m, and $\overline{S_w} = 8e - 04$. Observe how the trend in μ_f has indeed been smoothed by

the action of the white noise. This illustrates the impact of both red and white noise on the spectral moments within the analysis frame (i.e., changing cutoff frequency f_c). Similar results can be obtained for the bandwidth by carrying out the same analysis.

The bias term can take an arbitrary value depending on the noise variance and cutoff frequency, neither of which we know a priori. Consequently, for most real geological signals the mean frequency is situated off the main astronomical frequencies and the bandwidth encompasses a frequency band that seemingly does not fit to the physical reality. This aspect will be further illustrated and discussed in following sections.

Let us recall that the spectral moments describe the dynamics of the data as a whole and not of a single astronomical component. But after the initial calculations of the spectral moments, it can be useful to couple a spectral moment to a certain astronomical component. This is, for example, the case if one would like to reconstruct changes in sedimentation based on the spectral moments. Because of this bias caused by the presence of white noise, it is necessary to apply normalization to the spectral moments to be able to couple them to a given astronomical component. In this study we chose to normalize the smoothed trend of the bandwidth with a selected astronomical component to make the conversion from spectral moments to sedimentation rate estimates. This normalization is done at the beginning of the record; nevertheless, it can be done at an arbitrary depth as long as we identify a given orbital component. The smoothing of the trend in this study was done using the classical polynomial approximation in the framework of the overlap-add procedure (Verhelst, 2000). The selection of the astronomical component to couple the spectral moment is arbitrary but is best done with a component that is clearly present throughout the record.

3. Case Studies

3.1. Modified Insolation Signal

To introduce the reader with the new concepts of spectral moments in cyclostratigraphy, our first case study deals with a modified insolation signal (Figure 3a). The artificial input signal is the classic 65°N summer insolation for the last 6 Myr (Laskar et al., 2004; Milankovitch, 1941), with a red single to noise ratio of 1 ($\alpha = 0.9$ for red noise autocorrelation coefficient), a white signal to noise ratio of 3, conversion from time (sampling rate of 1 kyr) to distance domain by initially using a constant sedimentation rate of 2 cm/kyr (sampling rate of 0.02 m), and the introduction of a change in sedimentation rate using a second degree polynomial (Figure 3j). For the analytical expressions of the noise levels and the results of the same spectral moments analysis on the same insolation signal but for various noise scenarios, we refer to the supplementary information.

The periodogram of the detrended signal shows elevated power around frequencies of 1.2, 2, and 2.6 cycle/m (Figure 3b). Peaks in the spectrum below 1.2 cycle/m are due to the presence of the red noise that was not completely removed by detrending. The 1.2 and 2–2.6 cycle/m frequencies can be attributed to obliquity and precession, respectively. The spectrogram gives a similar image and also illustrates the increase in sedimentation rate toward greater depths, that is, component associated frequencies decrease with depth (Figure 3c). Also the amplitude-modulated effect of the precession component is clearly visible, including

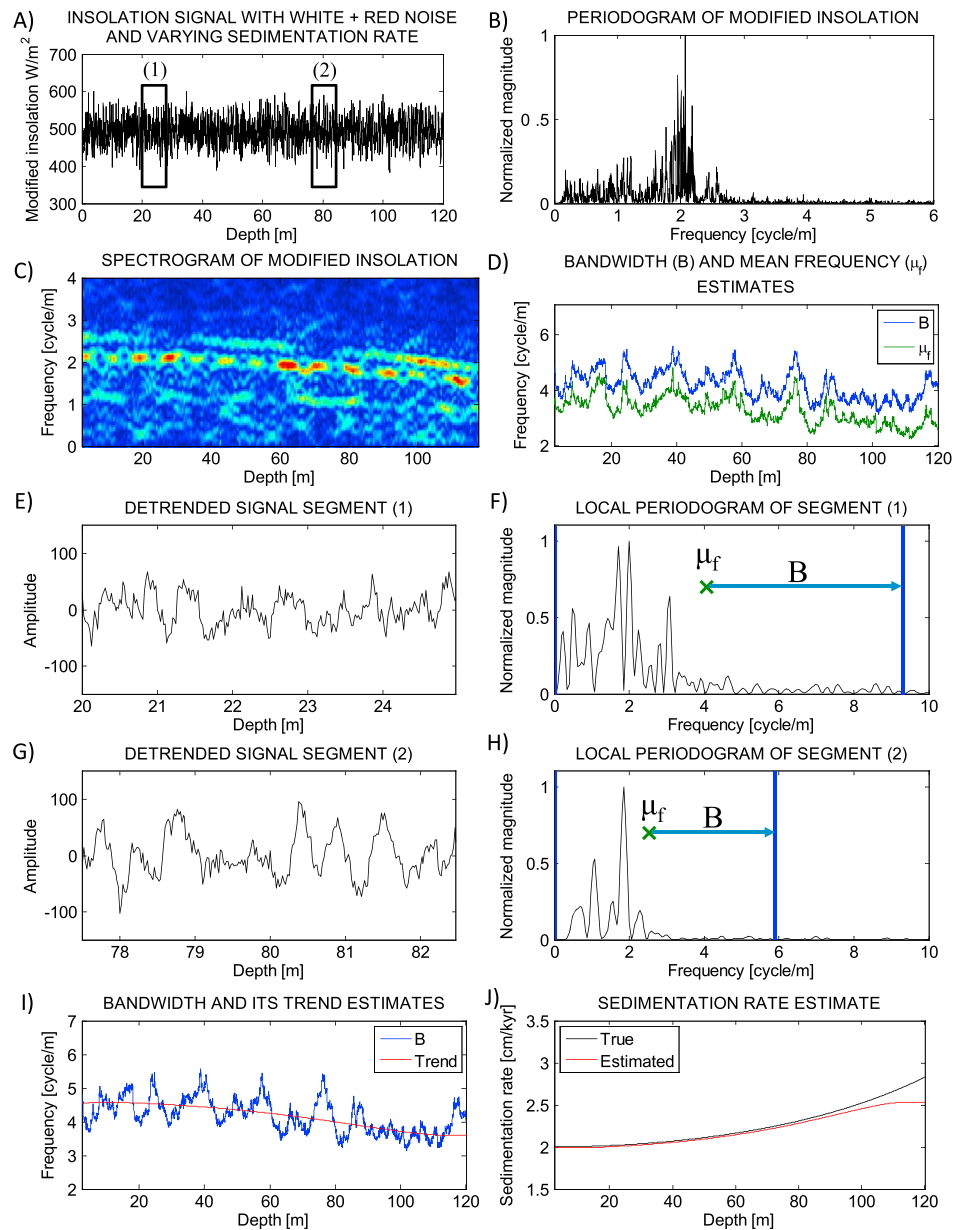


Figure 3. Spectral moment analysis for a synthetic insolation signal with a sampling rate of 0.02 m. (a) 6 Ma insolation for 65°N 21 June (W/m²) (Laskar et al., 2004) that is disturbed by adding red noise and white noise and a changing sedimentation rate. (b) The periodogram of the modified insolation signal as plotted in Figure 3a. (c) The spectrogram of the modified insolation signal. (d) The bandwidth (B) and mean frequency (μ) estimates for the modified insolation signal. (e) First 5 m segment (20–25 m) from the modified insolation signal. (f) The local periodogram of the first segment (Figure 3e) with indicated local B and μ . (g) Second 5 m segment (77–83 m) from the modified insolation signal. (h) The local periodogram of the second segment (Figure 3g) with indicated local B and μ . (i) The bandwidth and its trend estimate. (j) True and estimated sedimentation rate.

the merging of the 22 and 24-kyr periods into a single 23-kyr precession component (Figure 3c). This is the beating effect that originates in the presence of closely spaced sinusoidal components and accordingly generates the cross terms in the periodogram. This effect is illustrated in Figures 3e–3h where we see how the cross terms can substantially change the shape of the local periodogram on the frame basis.

The calculated spectral moments, bandwidth (B) and mean frequency (μ), have been calculated using a window size of 5 m and are shown in Figure 3d. Both moments show a similar course, that is, a slight decrease in values with depth, accompanied with variations around this decreasing trend of maximum amplitude of

2 cycle/m. These variations are less pronounced in the intervals 40–60 m and 100–120 m compared to the intervals 0–40 m and 60–100 m. This pattern follows the relative strengths of the 19 kyr and merged 23 kyr precession components, which is also modulated by the eccentricity. It is important to note that the visibility of this feature also depends on the selection of the window size, for example, these variations would be smoothed out when selected a much larger window size. To gain deeper insight into the values of the B and μ , we have selected two segments and plotted their respective spectral moments (Figures 3a, 3d, and 3e–3h). The first segment (Figure 3e, 20–25 m) has a μ of ~ 4 cycle/m and a B of ~ 5.5 cycle/m (Figure 3f), while the second segment (Figure 3g, 77–83 m) has a μ of ~ 2.5 cycle/m and a B of ~ 3 cycle/m (Figure 3h). As explained in section 2.3.3, the mean frequency (μ) and the size of the bandwidth (B) values do not accord, that is, have higher values, with the astronomical frequencies because of the noise bias. Opposite as one might expect, the B is not symmetric around the μ . This symmetry is actually only valid for symmetric probability density functions (e.g., normal or Gaussian distribution) and not for nonsymmetrical ones, like in our case the periodogram. Spectral moments can by definition not be negative and therefore the lower physical limit for the B is zero. When we take the (polynomial) long-term trend of the change in bandwidth (Figure 3i) and normalize this trend to the 41-kyr obliquity astronomical component (with a value around 1.2 cycle/m at 0 m) we get an estimation for the sedimentation rate. Here we chose to normalize against the obliquity component because it is a signal component in contrast with the different precession components that show beating effects, making the correct identification of its location in the spectrum less straightforward. The estimated sedimentation rate corresponds well to the true, modeled, change in sedimentation rate (Figure 3j).

3.2. IODP U1437

IODP site U1437 (31°47.39'N, 139°01.58'E) was drilled during IODP Expedition 350 *Izu-Bonin-Mariana Rear Arc*. Site U1437 is located in the Izu rear arc, in the North Western Pacific Ocean, close to the Izu volcanic front and continental Asia (Busby et al., 2017; Kars et al., 2017; Tamura et al., 2015). Site U1437 is under influence of westerly jet winds coming from continental Asia and the Kuroshio surface water current. Time series analysis by Kars et al. (2017) on NGR and rock magnetic properties of the first 120 m below sea floor (mbsf, sections U1437B 1H-1 through U1437B 17F-3) demonstrates a strong imprint of astronomical climate forcing and sea level changes on the mineralogy of the studied site for the last million years (1 Myr). These changes in mineralogy are hypothesized to reflect different origins of magnetic minerals, driven by monsoonal changes in eolian dust composition and supply (Kars et al., 2017).

We select Site U1437 as a case study for the illustration of the use of spectral moments in cyclostratigraphy, because of the strong astronomical imprint in this archive. As an input signal, we use the 10-cm spaced potassium (K) content series (in wt %) of the recovered, derived from the shipboard NGR data using the MATLAB algorithm by De Vleeschouwer et al. (2017). We consider the uppermost 160 mbsf of U1437B (Figure 4a). After detrending, both the periodogram (Figure 4b) and spectrogram (Figure 4c) are dominated by frequencies around 0.1 cycles/m. The periodogram also shows elevated power at other frequencies around 0.2, 0.3, 0.45, and 1.3 cycles/m (Figure 4b). The spectrogram shows that the 0.45 cycles/m frequency is the most consistent of these minor components over the analyzed record (Figure 4c). According to the interpretation of Kars et al. (2017), the 0.1 and 0.45 cycles/m frequencies correspond to the short 100-kyr eccentricity and 20-kyr precession astronomical periods. The spectrogram shows a “smearing of power” around 100 m and some elevated power around the aforementioned frequency of 1.3 cycles/m (Figure 4c). These are probably artifacts from a gap in the core recovery between 113.12 and 116.21 m in combination with the presence of the two peaks in K positioned at 102.11 and 111.51 m, which reflect volcanic ash layers (Figure 4a).

The bandwidth (B) and mean frequency (μ) of the K (wt %) depth series were calculated using a window of 20 m and are plotted in Figure 4d. Both have a value that varies around 1 cycle/m throughout the record. Two remarkable sharp transitions for the two spectral moments occur around 100 and 120 m, which are also related to the presence of the two volcanic ash layers. This is an illustration on how the spectral moment approach has the potential to detect irregularities in a paleoclimate record, without a priori data processing. The ash layers in the U1437 sedimentary record, manifested by high K content, obviously do not represent a climatic signal. To further investigate the behavior of both spectral moments, we removed the ash layers from the K depth series (Figure 4e) and recalculated B and μ (Figure 4f). The resulting evolution of B and μ as a function of depth is much smoother in the 100–120 m interval compared to Figure 4d. Nevertheless, some rather

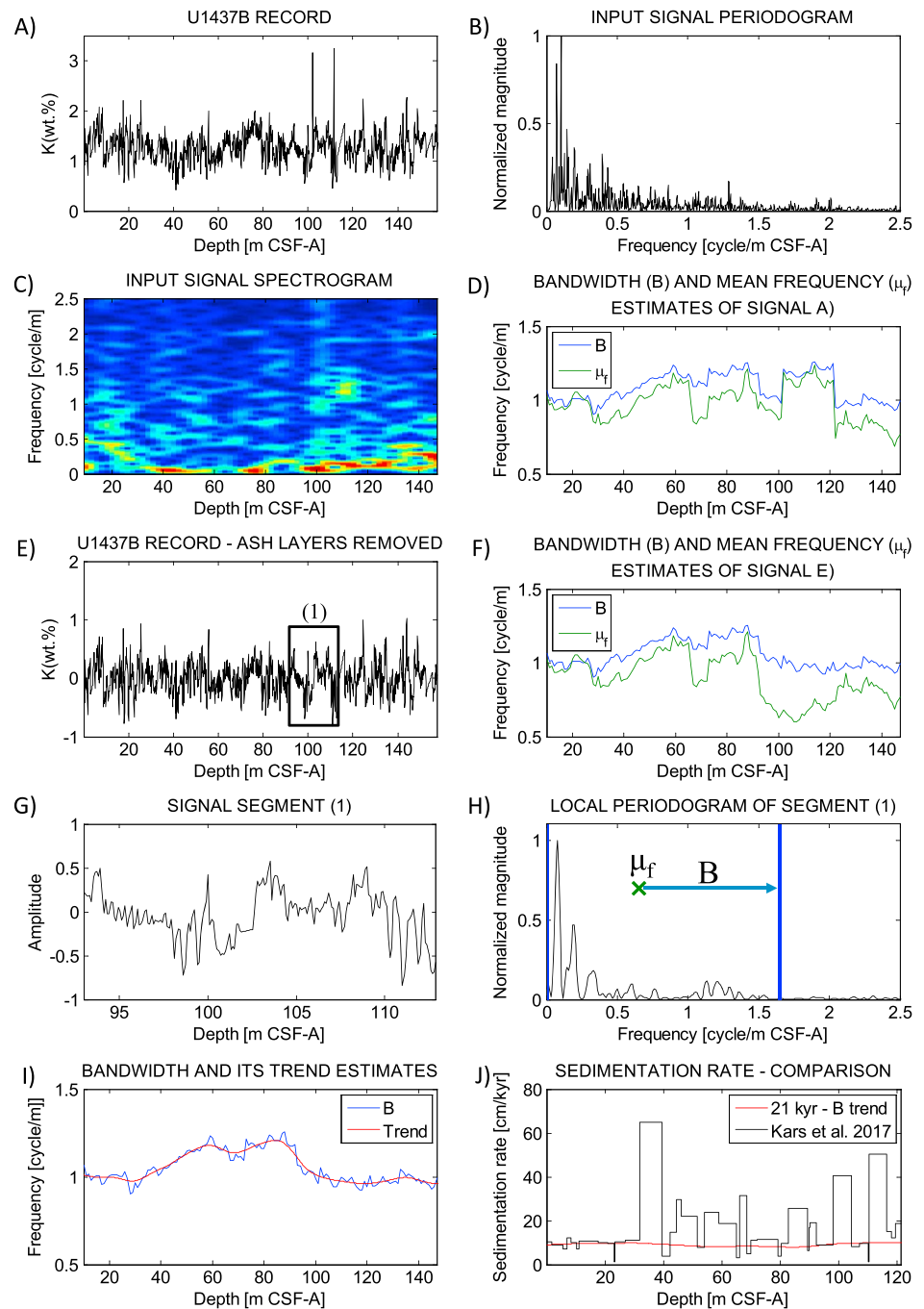


Figure 4. Spectral moment analysis for the U1437B NGR-derived K (wt%) record that has an average sampling rate of ~ 0.10 m. (a) U1437B K (wt %) record, quantified using the algorithm of De Vleeschouwer et al. (2017). (b) The periodogram of K (wt %) record as plotted in Figure 4a. (c) The spectrogram of the K (wt %) record. (d) The bandwidth (B) and mean frequency (μ_f) estimates for the K (wt %) record. (e) U1437B K (wt %) record without the presence of ash layers. (f) The bandwidth (B) and mean frequency (μ_f) estimates for the K (wt %) record without ash layers. (g) First 20-m segment (93–113 m) from the K (wt %) record. (h) The local periodogram of the first segment (Figure 4g) with indicated local B and μ_f . (i) The bandwidth and its trend estimate. (j) Estimated sedimentation rates from the precession estimate and the Kars et al. (2017) age model.

rapid changes in B and μ_f still occur. For example, a sharp transition from lower to higher values occurs around 90 m. This transition was previously masked in the analysis including the volcanic K peaks (Figure 4d) but corresponds to a noteworthy decrease in sedimentation rate (Figure 4j).

We illustrate how spectral moments relate to the periodogram by plotting B and μ for a 20-m long segment (Figure 4g) in Figure 4h. As explained in the section 2, the spectral moments do not coincide with the frequencies with elevated power because of the presence of noise.

We smoothed the B curve using the overlap-add method, and to test the hypothesis that the phase contribution is related to changes in sedimentation rate, we rescaled the precession component at $0.45 \text{ cycle m}^{-1}$ and assigning a duration of 21 kyr to this spatial frequency (Figure 4j). In this case study we scaled to the precession component because it is the most consistent one over the record and in contrast with the previous case study that only resolved as a single component. Subsequently, we evaluate our sedimentation rate estimates with the previously published sedimentation rate curve, derived from the Kars et al. (2017) age model (Figure 4j). The Kars et al. (2017) age model is based on the identification of 2 magnetostratigraphic boundaries, 4 calcareous nannofossil datums, and 38 depth-to-time tie points, identified by tuning the planktonic foraminifera *Neoglobobulimina dutertrei* $\delta^{18}\text{O}$ curve (Mloneck-Vautrayers, 2018) to the benthic $\delta^{18}\text{O}$ LR04 stack (Lisiecki & Raymo, 2005). The average sedimentation rate of this study ($\sim 10 \text{ cm/kyr}$) is slightly lower but in good agreement with the average sedimentation rate from Kars et al. (2017; $\sim 11 \text{ cm/kyr}$), as well as with the shipboard age model ($\sim 12 \text{ cm/kyr}$; Tamura et al., 2015). The Kars et al. (2017) age model, however, is characterized by much stronger variability in sedimentation rate. These authors report sedimentation rates ranging between 1.18 and 65.04 cm/kyr, whereas in this study, we report a much smoother sedimentation rate evolution. This difference is explained in two ways: First, the approach in this study is designed to capture the main trend in sedimentation rate changes and does not allow for precise fine tuning, requiring fast changes in sedimentation rate. Second, certain isotopic tie points for the Kars et al. (2017) age model are taken at low-resolution intervals in the $\delta^{18}\text{O}$ curve, making the correlation with the LR04 stack more challenging.

Overall, this case study exemplified how the spectral moments can indicate important features in the data prior to cyclostratigraphic analysis (in this particular case, the presence of volcanic ash layers) and how the relative variation of the spectral moments over the record can be used for estimating trends in sedimentation rate changes over a record.

3.3. ODP982

The $\delta^{18}\text{O}$ of benthic foraminifer tests is a well-established proxy in paleoclimate research, as it reflects a combination of Earth's average temperature and size of the cryosphere (e.g., Emiliani, 1954; Pearson, 2012). These characteristics make that this proxy is particularly suitable as a recorder of astronomical climate forcing (e.g., Hays et al., 1976; Lisiecki & Raymo, 2005). The next two case studies will display different features of using spectral moments on two of this sort of benthic oxygen isotope records. The first record comes from ODP Site 982 from the North Atlantic ($57^{\circ}30.8'\text{N}$, $15^{\circ}52.5'\text{W}$; Venz et al., 1999; Venz & Hodell, 2002; Lisiecki & Raymo, 2005). The ODP 982 benthic $\delta^{18}\text{O}$ record (average sampling rate of $\sim 0.05 \text{ m}$) is used in the reference Pliocene-Pleistocene stack by Lisiecki and Raymo (2005).

After detrending the record (Figure 5a), the global periodogram mainly shows elevated power for several peaks between 0 and 0.5 cycles/m, and to a lesser extent to frequencies around 1 and 1.5 cycles/m (Figure 5b). According to the Lisiecki and Raymo (2005) age model for this record, the 1-cycles/m frequency reflects obliquity and the high-power frequency at $\sim 0.5 \text{ cycles/m}$ relates to the 100-kyr short eccentricity. The spectrogram does not show stable and clearly traceable components (Figure 5c) because much of the power of the spectrogram is concentrated in the uppermost 30 m. Here high-amplitude variations in the $\delta^{18}\text{O}$ signal overwhelm the power spectrum of the lower part of the signal (Figure 5c). In addition, the original sample frequency shifts halfway the record from every 5 cm to every 20 cm causing a reduction in signal resolution—the sample frequency however still respects the theoretical minimum condition of the Nyquist frequency for the detection of all astronomical components.

The B and μ , calculated using a window size of 25 m, both show a steady increase from a value around 0.5 till 1.5 cycles/m from the bottom of the record till 30 m depth, where after there is a decrease toward a value around 1.0 cycles/m (Figure 5d). Figures 5e–5h illustrate the difference in periodograms and spectral moment characteristics between the intervals with maximal and minimal values for B and μ . For the maximal values (Figures 5e and 5f), the spectrum is broader, while the spectrum for the minimal values is narrower and more concentrated in the lower frequency range (Figures 5g and 5h). We estimate the trend in sedimentation rate by taking the trend of the B and scaling it to the 41-kyr obliquity component that has at the top of the core a

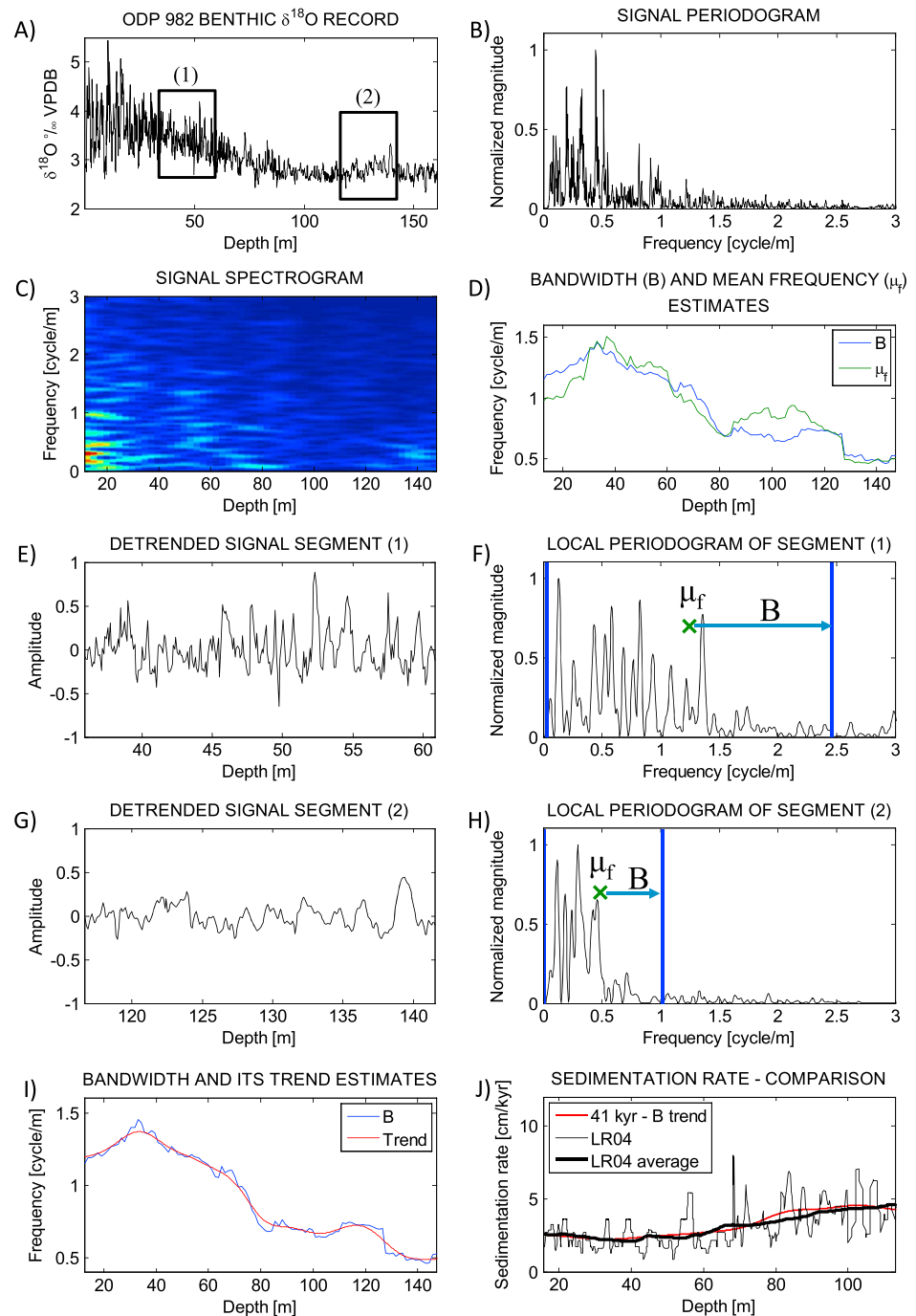


Figure 5. Spectral moment analysis for the ODP 982 benthic $\delta^{18}\text{O}$ record that has an average sampling rate of ~ 0.05 m. (a) ODP 982 benthic $\delta^{18}\text{O}$ record from Venz et al. (1999) and Venz and Hodell (2002). (b) The periodogram of the ODP 982 benthic $\delta^{18}\text{O}$ record as plotted in Figure 5a. (c) The spectrogram of the ODP 982 benthic $\delta^{18}\text{O}$ record. (d) The bandwidth (B) and mean frequency (μ) estimates for the ODP 982 benthic $\delta^{18}\text{O}$ record. (e) First 25 m segment (36–61 m) from the ODP 982 benthic $\delta^{18}\text{O}$ record. (f) The local periodogram of the first segment (Figure 5e) with indicated local B and μ . (g) Second 25 m segment (116–141 m) from the ODP 982 benthic $\delta^{18}\text{O}$ record. (h) The local periodogram of the second segment (Figure 5g) with indicated local B and μ . (i) The bandwidth and its trend estimate. (j) Estimated sedimentation rates from the obliquity estimate and the Lisiecki and Raymo (2005) age model.

frequency of ~ 1 cycles/m (Figures 5i and 5j). Compared to the sedimentation rates derived from the Lisiecki and Raymo (2005) age model, this approach fails at picking up fast changes in sedimentation rate but again reconstruct the trend in change of sedimentation rate well (Figure 5j).

The sedimentation rate halves over the record from an average at the base of about 4 cm/kyr to about 2 cm/kyr (Figure 5j). This means that the signal in the depth domain is highly nonstationary, and that for example the location of the obliquity component in the spectrogram shifts over the record from 0.6 to 1.2 cycle/m (Figures 5b and 5c). Such significant changes in sedimentation rate strongly complicate the astronomical interpretation of a paleoclimate record. For instance, the astronomical component estimation model (ACE v1, Sinnesael et al., 2016) assumes no overlap between the frequency ranges of analyzed astronomical components. The spectral moment approach is however not hampered by overlapping component frequency ranges. This characteristic illustrates an important merit of the spectral moment approach in cyclostratigraphy applications. The spectral moment approach seems particularly useful as a first processing step, after which other existing techniques can be applied for further fine tuning.

3.4. ODP677

The second investigated benthic oxygen isotope record spans the entire Quaternary at ODP Site 677, drilled in the equatorial East Pacific (1°12'N, 83°44'W; Becker et al., 1988). Shackleton and Hall (1989) generated a first high-resolution benthic oxygen isotope record for this site, and its astronomical calibration was discussed by Shackleton et al. (1990). The Site 677 record (average sampling rate of ~0.10 m) is also incorporated in the LR04 stack, which provides the age model for comparison with this study's results.

The main frequencies with elevated power are around 0.22, 0.54, and to a lesser extent 1.11 cycles/m (Figures 6a and 6b). Using the Lisiecki and Raymo (2005) age model, these periods can respectively be associated with the astronomical short eccentricity, obliquity, and precession components. The spectrogram shows a clear distinction between the obliquity and the eccentricity component in the upper part of the record (0–50 m), but this distinction gets obscured in the lower part of the record (50–100 m; Figure 6c). Another characteristic of the spectrogram is the elevated power in the short eccentricity frequency range for the upper 30 to 40 m. The B and μ , using a window of 25 m for the calculations, are relatively stable for the lower part (50–100 m) and decrease from 50 m till the top of the record (Figure 6d). Figures 6e–6h illustrate the difference of the spectrum characteristics and corresponding spectral moments between the so-called 100-kyr and 41-kyr worlds. The stronger 100-kyr cycle shifts the spectral moments to lower values. Accordingly, when the trend in B is used to derive an estimate in sedimentation rate for the ODP677 record, the model suggests an increase in sedimentation rate for the interval with the stronger 100-kyr cycle (Figures 6i and 6j). Comparing this estimated sedimentation rate with the Lisiecki and Raymo (2005) age model-derived sedimentation rate shows a significant offset up to 2 cm/kyr (Figure 6j). This means that for this case study, the change in spectral moments was not (only) related to changes in sedimentation rate but more by a shifting energy level of different astronomical components in the studied signal. In other words, the climatic transition from the 41-kyr to the 100-kyr world (i.e., the Mid-Pleistocene transition) is visible in the spectral moment evolution. The same phenomenon was also visible for the ODP982 record where there was a decrease in B and μ for the last 30 m, which correspond with the 100-kyr world. The spectral moments of a depth series are thus significantly influenced by a shift in climate dynamics like the Mid-Pleistocene transition, during which glacial-interglacial variability switch from a 40-kyr to a 100-kyr period. In other words, spectral moments do not only trace changes in sedimentary rate but also changes in the climate system's response to astronomical forcing.

4. Discussion

There is often a trade-off between simplicity and accuracy. The presented study focuses on the simplicity component. The new idea presented here is to look at the characteristics of a whole spectrum and not only of single component. Spectral moments “an sich” can be calculated for any record. Interpretations and potential applications depend on the specific context and the question asked. Sensible interpretations of the numbers without any a priori knowledge of the broader geological context (e.g., proxy understanding, sedimentology, biostratigraphy, magnetostratigraphy, and chemostratigraphy) can be problematic. The quality and resolution of available (contextual) information of a signal are however highly variable. Often some information is available and one has some rough ideas on a section or signal (e.g., approximate stratigraphic interval and order of magnitude of time in studied interval) but one lacks the higher resolution information (which still can contain considerable

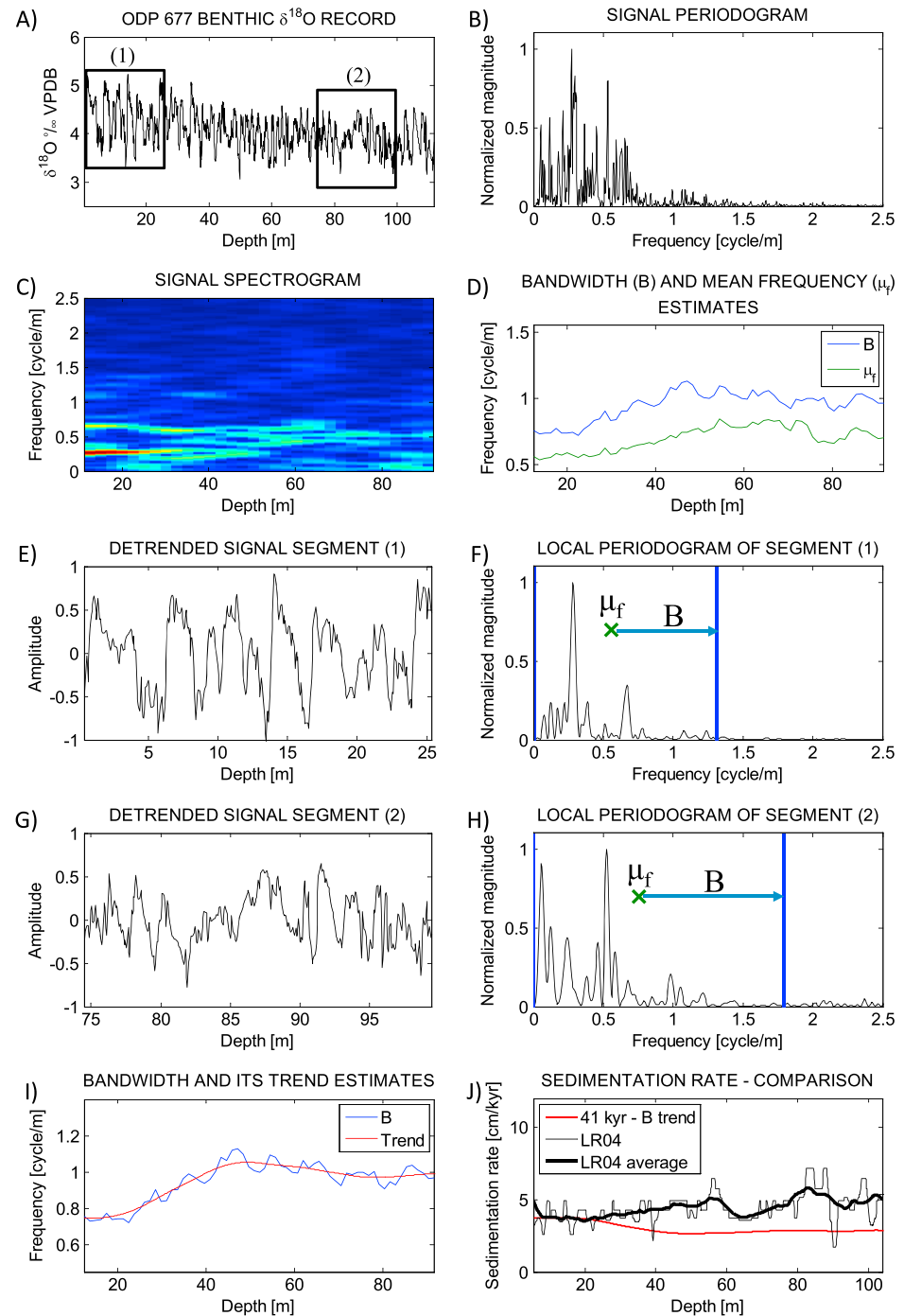


Figure 6. Spectral moment analysis for the ODP 677 benthic $\delta^{18}\text{O}$ record that has an average sampling rate of ~ 0.10 m. (a) ODP 677 benthic $\delta^{18}\text{O}$ record from Shackleton and Hall (1989). (b) The periodogram of the ODP 677 benthic $\delta^{18}\text{O}$ record as plotted in Figure 6a. (c) The spectrogram of the ODP 677 benthic $\delta^{18}\text{O}$ record. (d) The bandwidth (B) and mean frequency (μ) estimates for the ODP 677 benthic $\delta^{18}\text{O}$ record. (e) First 25 m segment (0–25 m) from the ODP 677 benthic $\delta^{18}\text{O}$ record. (f) The local periodogram of the first segment (Figure 6e) with indicated local B and μ . (g) Second 25-m segment (75–100 m) from the ODP 677 benthic $\delta^{18}\text{O}$ record. (h) The local periodogram of the second segment (Figure 6g) with indicated local B and μ . (i) The bandwidth and its trend estimate. (j) Estimated sedimentation rates from the obliquity estimate and the Lisiecki and Raymo (2005) age model.

variability). In such cases, we suggest that the application of spectral moments can be useful as the technique looks at how the spectrum of a signal changes over the record (e.g., due to changes in sedimentation rate or due to a change in climate sensitivity to astronomical forcing). The spectral moment technique is mathematically simple and does not require much user-defined settings (except for the analysis window size).

The case studies illustrated several merits and drawbacks of the application of spectral moments in cyclostratigraphy. All four case studies showed the potential for the reconstruction of main patterns in sedimentation rates by tracking the change in spectral moments in a record. It should be noted that other, existing, techniques can be used to further fine-tune sedimentation rate estimates after the main trend has been captured with the spectral moment approach suggested in this study. But the spectral moments approach can be used for much more than only sedimentation rate reconstruction—and one has to consider that certainly not all changes in spectral moment distribution are caused by changes in sedimentation rate. The ODP677 benthic $\delta^{18}\text{O}$ study showed how the increase in power of the 100-kyr component relative to the obliquity component during the Mid-Pleistocene transition shifted the spectral moments to lower values. This shift reflected a change in climate response to astronomical forcing rather than a change in sedimentation. The spectral moments of the modified insolation signal showed the AM of precession by eccentricity (given a window size that allows for its detection). Also anomalous values, like for example the volcanic ashes for the U1437B case study, can cause sudden changes in spectrum characteristics that can be picked up by the spectral moments. As such, looking at the evolution of the properties of the full spectrum, and not only single components, can serve as a valuable first step in processing and gaining insight in the features of a particular data record. As indicated in the first paragraph of section 4, cross-checking with potential other sources of information stays necessary to be able to convincingly distinguish between various changes in the spectral moments.

There are however certain conditions and limitations to the application of this approach too. Nonuniform sampling rates of an analyzed record can complicate the interpretation of the changes in spectrum characteristics. Imagine one increases the sampling rate over a record. As a consequence, the power at higher frequencies will increase and shift the values of the calculated spectral moments to higher values. Interpreting this shift as a result of changing paleoclimatological or sedimentological conditions would be incorrect, as it is only due to a different resolution in sampling. A changing sampling rate, assuming a constant sedimentation rate, might also have as an effect that the Nyquist condition (minimal sampling rate) for a certain period is no longer respected (or vice versa). Alternatively, can large changes in sedimentation rate for a constant sampling rate have a similar effect? Another complication appears when dealing with a relative pure signal (narrow band pass). In this case the assumption of a broad power spectrum, which is the basis of the spectral moments approach, will not be valid as pure signals have a narrow power spectra. An analysis of a band-pass signal returns more-or-less constant bandwidth and the correct mean frequency. What is the reason for this? Let us assume that the sedimentation rate decreases, and then individual components move up to higher frequencies in the periodogram. In a low-pass signal, this is viewed as a spectrum expanding. Therefore, there are two effects: shifting and expanding. In a band-pass signal scenario the shifting is much stronger than the expanding. Therefore, the bandwidth would not change much while the mean frequency will nicely follow the sedimentation rate dynamics. We also saw how the presence of noise shifts the frequencies of the spectral moments to higher frequencies than the actual orbital components. This is something the spectral moments cannot deal with, unless one would consider an additional processing step that would estimate the signal-to-noise ratio at each analysis frame.

This study demonstrated some interesting applications of the spectral moments technique and also touched upon some open questions. We used the periodogram as density function, but this might not be the ideal spectral technique to use in combination with spectral moments. What would for example happen if one would use the commonly used multitaper method (MTM, Thomson, 1982) instead of the periodogram? The MTM is often preferred over the periodogram because it has a superior capability to bring out singular (sinusoidal) components against the continuous spectral background (noise). The approach in this study is however to consider the whole spectrum and not only individual components, making the MTM lose its particular advantage over the periodogram. Nevertheless, experimenting with other density function might be valuable. Besides the actual choice of the density function, the way this function is characterized might be even more important. We proposed the first two spectral moments, the mean frequency (μ) and

bandwidth (B), but other ways of describing an energy distribution exist too (e.g., higher-order central moments like skewness and kurtosis, or principles like spectral flatness or Wiener entropy). Additional work can also consider studying in more detail the effect of various noise distributions over a record, for example, seek for ways to deal with nonstationary noise over a signal. Another path to explore would be the integration of any a priori information or assumptions that might constrain the outcome.

5. Conclusions

The main contribution of this work is raising awareness for a new way of thinking to characterize time series of paleoclimate data: namely, considering the use of broadband or full spectrum properties to describe a signal instead of looking solely at single components. We initially evaluate the use of a periodogram with its two first spectral moments, mean frequency (μ) and bandwidth (B), with a moving window approach to investigate the analyzed records. Respecting some conditions and limitations, the results of the case studies demonstrated the potential of this spectral moment approach as a valuable first step in processing and gaining insight in the features of a particular data record. This initial processing step is meant to be complementary to existing approaches. General principles regarding the quality of the analyzed data and respecting available additional constraints while interpreting the results remain indispensable. Besides describing variation of a signal, this study also shows that this approach can be used to reconstruct first-order changes in sedimentation rate.

Appendix A

In the present Appendix A we show the intermediate steps from (equation (13)), leading to equations (14) and (15) for a case of two signal component—which can be extended to a general multicomponent signal.

According to equation (13) a two-component discrete signal can be written as

$$s(z_n) = \sum_{j=1}^2 s_j(z_n) = s_1(z_n) + s_2(z_n), \quad n = 1, \dots, N. \quad (\text{A1})$$

By applying the DFT to the previous expression we obtain the relationship between the corresponding discrete spectra:

$$\zeta(f_k) = \zeta_1(f_k) + \zeta_2(f_k), \quad k = 1, \dots, K, \quad (\text{A2})$$

where the symbol ζ stands for the DFT evaluated at the discrete frequencies f_k . The periodogram $S(f_k)$ of the input data is represented in terms of the constituent spectra:

$$\begin{aligned} S(f_k) &= |\zeta(f_k)|^2 = \zeta^*(f_k) \zeta(f_k) = (\zeta_1^*(f_k) + \zeta_2^*(f_k))(\zeta_1(f_k) + \zeta_2(f_k)) = \\ &= \zeta_1^*(f_k) \zeta_1(f_k) + \zeta_2^*(f_k) \zeta_2(f_k) + \zeta_1^*(f_k) \zeta_2(f_k) + \zeta_2^*(f_k) \zeta_1(f_k), \end{aligned} \quad (\text{A3})$$

with the symbol “*” stands for the complex conjugate operator. In (A3) the first two terms are equal to the individual periodograms $S_1(f_k)$ and $S_2(f_k)$, respectively. To calculate the cross terms, let us first write the individual spectra in the complex form:

$$\zeta_1(f_k) = \zeta_{1,R}(f_k) + j\zeta_{1,I}(f_k), \quad (\text{A4.1})$$

$$\zeta_2(f_k) = \zeta_{2,R}(f_k) + j\zeta_{2,I}(f_k). \quad (\text{A4.2})$$

Combining (A3) with (A4.1) and (A4.2) we obtain the expression (equation (15)) for the cross terms:

$$\begin{aligned} \zeta_1^*(f_k) \zeta_2(f_k) + \zeta_2^*(f_k) \zeta_1(f_k) &= 2(\zeta_{1,R}(f_k) \zeta_{2,R}(f_k) + \zeta_{1,I}(f_k) \zeta_{2,I}(f_k)) = \\ &= 2\Re\{\zeta_1^*(f_k) \zeta_2(f_k)\}. \end{aligned} \quad (\text{A5})$$

with “ \Re ” represents the real part of a complex value.

Appendix B

In the present Appendix B we show the computation steps leading to equation (22). Denoting $\overline{S_w} = \sigma_w^2 / f_s = \text{Const}$ the noise level in the periodogram, the mean frequency of the white noise in the frequency range $[f_c, f_s]$ is according to equation (20):

$$\mu_{f,w} = \sum_{k=c}^N f_k S_w(f_k) = \overline{S_w} \sum_{k=c}^N f_k = \overline{S_w} \frac{f_s}{2N} \sum_{k=c}^N k \quad (\text{B1})$$

given $f_k = k\Delta f$, where $\Delta f = f_s/2N$ is the resolution of the FFT. To calculate the sum in (B1), we make use of the following identity:

$$\sum_{k=1}^N k = \frac{N(N+1)}{2} \quad (\text{B2})$$

Accordingly, we rewrite (B1) as

$$\mu_{f,w} = \overline{S_w} \frac{f_s}{2N} \left[\frac{N(N+1) - c(c+1)}{2} \right] = \overline{S_w} \frac{f_s}{4N} [N^2 - c(c+1)] \quad (\text{B3})$$

In the last expression we assume that $N \gg 1$ that is normally satisfied. Finally, assuming that $\mu_{f,0r} = f_c/2 = cf_s/4N$ and together with (B3) we come up with expression (equation (22)).

Acknowledgments

Matthias Sinnesael thanks the Research Foundation of Flanders (FWO) for the awarded PhD Fellowship (FWOTM782). David De Vleeschouwer was funded through European Research Council (ERC) Consolidator Grant "Earthsequencing" (grant agreement 617462). We thank Jiri Laurin for the constructive review, which helped to improve this manuscript. The original data that we used for the real case studies are available in following online repositories. For the first case study on IODP U1437 on the natural gamma ray record, the data can be found in the IEDA repository: <http://get.iedadata.org/doi/100668> (De Vleeschouwer et al., 2017). For the second case study on ODP 982 benthic oxygen isotope record, the original data can be found at the PANGAEA depository: <https://doi.pangaea.de/10.1594/PANGAEA.700897?format=html#download> (Venz et al., 1999) and <https://doi.pangaea.de/10.1594/PANGAEA.774880> (Venz & Hodell, 2002). The benthic oxygen isotope data from the third case study from ODP677 is also available from the PANGAEA database: <https://doi.pangaea.de/10.1594/PANGAEA.701308> (Shackleton & Hall, 1989). The LR04 age model can be found at the PANGAEA depository (<https://doi.pangaea.de/10.1594/PANGAEA.704257>) and the following website (<http://lorraine-lisiecki.com/stack.html>) that also include the individual records for each site (Lisiecki & Raymo, 2005). MATLAB scripts that are used to calculate the spectral moments are made fully available in the supporting information.

References

- Becker, K., Sakai, H., Merrill, R. B., Adamson, A. C., Alexandrovich, J., Alt, J. C., et al. (1988). Initial reports. In *Proceedings of the Ocean Drilling Program: Scientific results* (Vol. 111, pp. 295–316). College Station, TX: Ocean Drilling Program. <https://doi.org/10.2973/odp.proc.ir.111.1988>
- Berger, A. L. (1978). Long-term variations of daily insolation and Quaternary climatic changes. *Journal of the Atmospheric Sciences*, 35(12), 2362–2367. [https://doi.org/10.1175/1520-0469\(1978\)035%3C2362:LTVDI%3E2.0.CO;2](https://doi.org/10.1175/1520-0469(1978)035%3C2362:LTVDI%3E2.0.CO;2)
- Betser, M., Collen, P., Richard, G., & David, B. (2008). Estimation of frequency for AM/FM models using the phase vocoder framework. *IEEE Transactions on Signal Processing*, 56(2), 505–517. <https://doi.org/10.1109/TSP.2007.906768>
- Boashash, B. (1992). Estimating and interpreting the instantaneous frequency of a signal. I. Fundamentals. *Proceedings of the IEEE*, 80(4), 520–538. <https://doi.org/10.1109/5.135376>
- Busby, C. J., Tamura, Y., Blum, P., Guérin, G., Andrews, G. D. M., Barker, A. K., et al. (2017). The missing half of the subduction factory: Shipboard results from the Izu rear arc, IODP Expedition 350. *International Geology Review*, 59(13), 1677–1708. <https://doi.org/10.1080/00206814.2017.1292469>
- Cohen, L. (1995). *Time-frequency analysis: Theory and applications* (299 pp.). NJ: Prentice Hall.
- De Vleeschouwer, D., Dunlea, A. G., Auer, G., Anderson, C. H., Brumsack, H., de Loach, A., et al. (2017). Quantifying K, U, and Th contents of marine sediments using shipboard natural gamma radiation spectra measured on DV JOIDES Resolution. *Geochemistry, Geophysics, Geosystems*, 18, 1053–1064. <https://doi.org/10.1002/2016GC006715>
- Emiliani, C. (1954). Temperatures of Pacific bottom waters and polar superficial waters during the Tertiary. *Science*, 119(3103), 853–855. <https://doi.org/10.1126/science.119.3103.853>
- Gazor, S., & RashidiFar, R. (2006). Adaptive maximum windowed likelihood multicomponent AM-FM signal decomposition. *IEEE Transactions on Audio, Speech and Language Processing*, 14(2), 479–491. <https://doi.org/10.1109/TSA.2005.857808>
- Hays, J. D., Imbrie, J., & Shackleton, N. J. (1976). Variations in the Earth's orbit: Pacemaker of the ice ages. *Science*, 194(4270), 1121–1132. <https://doi.org/10.1126/science.194.4270.1121>
- Hinnov, L. A. (2013). Cyclostratigraphy and its revolutionizing applications in the Earth and planetary sciences. *Geological Society of America Bulletin*, 125(11–12), 1703–1734. <https://doi.org/10.1130/B30934.1>
- Hinnov, L. A., & Hilgen, F. J. (2012). Cyclostratigraphy and astrochronology. In F. M. Gradstein, J. G. Ogg, M. D. Schmitz, & G. M. Ogg (Eds.), *The geological time scale 2012* (pp. 63–84). Amsterdam: Elsevier.
- Imbrie, J. (1982). Astronomical theory of the Pleistocene ice ages: A brief historical review. *Icarus*, 50(2–3), 408–422. [https://doi.org/10.1016/0019-1035\(82\)90132-4](https://doi.org/10.1016/0019-1035(82)90132-4)
- Kars, M., Musgrave, R. J., Kodama, K., Jonas, A.-S., Bordiga, M., Ruebsam, W., et al. (2017). Impact of climate change on the magnetic mineral assemblage in marine sediments from Izu rear arc, NW Pacific Ocean, over the last 1 Myr. *Palaeogeography, Palaeoclimatology, Palaeoecology*, 480, 53–69. <https://doi.org/10.1016/j.palaeo.2017.05.016>
- Laskar, J., Robutel, P., Joutel, F., Gastineau, M., Correia, A. C. M., & Levrard, B. (2004). A long-term numerical solution for the insolation quantities of the Earth. *Astronomy and Astrophysics*, 428(1), 261–285. <https://doi.org/10.1051/0004-6361:20041335>
- Li, M., Hinnov, L. A., Huang, C., & Ogg, J. G. (2018). Sedimentary noise and sea levels linked to land-ocean water exchange and obliquity forcing. *Nature Communications*, 9(1), 1004. <https://doi.org/10.1038/s41467-018-03454-y>
- Lisiecki, L. E., & Raymo, M. E. (2005). A Pliocene-Pleistocene stack of 57 globally distributed benthic $\delta^{18}\text{O}$ records: Pliocene-Pleistocene benthic stack. *Paleoceanography*, 20, PA1003. <https://doi.org/10.1029/2004PA001071>
- Loughlin, P. J., & Tacer, B. (1996). On the amplitude and frequency modulation decomposition of signals. *The Journal of the Acoustical Society of America*, 100(3), 1594–1601. <https://doi.org/10.1121/1.416061>
- Mann, M. E., & Lees, J. M. (1996). Robust estimation of background noise and signal detection in climatic time series. *Climatic Change*, 33(3), 409–445. <https://doi.org/10.1007/BF00142586>
- Meyers, S. R. (2012). Seeing red in cyclic stratigraphy: Spectral noise estimation for astrochronology. *Paleoceanography*, 27, PA3228. <https://doi.org/10.1029/2012PA002307>

- Meyers, S. R., & Sageman, B. B. (2007). Quantification of deep-time orbital forcing by average spectral misfit. *American Journal of Science*, 307(5), 773–792. <https://doi.org/10.2475/05.2007.01>
- Meyers, S. R., Sageman, B. B., & Arthur, M. A. (2012). Obliquity forcing of organic matter accumulation during Oceanic Anoxic Event 2: Obliquity forcing during OAE 2. *Paleoceanography*, 27, PA3212. <https://doi.org/10.1029/2012PA002286>
- Meyers, S. R., Sageman, B. B., & Hinnov, L. A. (2001). Integrated quantitative stratigraphy of the Cenomanian-Turonian Bridge Creek limestone member using evolutive harmonic analysis and stratigraphic modeling. *Journal of Sedimentary Research*, 71(4), 628–644. <https://doi.org/10.1306/012401710628>
- Meyers, S. R., Sageman, B. B., & Pagani, M. (2008). Resolving Milankovitch: Consideration of signal and noise. *American Journal of Science*, 308(6), 770–786. <https://doi.org/10.2475/06.2008.02>
- Milankovitch, M. (1941). *Kanon der Erdbestrahlung und seine Auswirkung auf das Eiszeitenproblem* (633 pp.). Belgrad, Edit. Spec. 133: Königlich Serbische Akademie.
- Mleneck-Vautrayers, M. J. (2018). Quantitative planktonic foraminifers taphonomy and paleoceanographic implications over the last 1 Myr from IODP sites U1436 and U1437. *Cogent Geoscience*, 4(1), 1447263. <https://doi.org/10.1080/23312041.2018.1447263>
- Muller, R. A., & MacDonald, G. J. (2000). *Ice ages and astronomical causes*. *Data, Spectral Analysis and Mechanisms* (318 pp.). London: Springer.
- Pantazis, Y., Rosenc, O., & Stylianou, Y. (2011). Adaptive AM-FM signal decomposition with application to speech analysis. *IEEE Transactions on Audio, Speech and Language Processing*, 19(2), 290–300. <https://doi.org/10.1109/TASL.2010.2047682>
- Pearson, P. N. (2012). Oxygen isotopes in foraminifera: Overview and historical review. *Paleontological Society Papers*, 18, 1–38. <https://doi.org/10.1017/S1089332600002539>
- Quatieri, T. F., Hanna, T. E., & O'Leary, G. C. (1997). AM-FM separation using auditory-motivated filters. *IEEE Transactions on Speech and Audio Processing*, 5(5), 465–480. <https://doi.org/10.1109/89.622571>
- Shackleton, N. J., Berger, A., & Peltier, W. R. (1990). An alternative astronomical calibration of the lower Pleistocene timescale based on ODP site 677. *Transactions of the Royal Society of Edinburgh: Earth Sciences*, 81(04), 251–261. <https://doi.org/10.1017/S0263593300020782>
- Shackleton, N. J., & Hall, M. A. (1989). 25. Stable isotope history of the Pleistocene at ODP site 677. In *Proceedings of the Ocean Drilling Program: Scientific results* (Vol. 111, pp. 295–316). College Station, TX: Ocean Drilling Program.
- Sinnesael, M., Zivanovic, M., De Vleeschouwer, D., Claeys, P., & Schoukens, J. (2016). Astronomical component estimation (ACE v.1) by time-variant sinusoidal modeling. *Geoscientific Model Development*, 9(10), 3517–3531. <https://doi.org/10.5194/gmd-9-3517-2016>
- Tamura, Y., Busby, C. J., Blum, P., & the Expedition 350 Scientists (2015). Site U1437. *Proceedings of the International Ocean Discovery Program* (Vol. 50, 142 pp.). <https://doi.org/10.14379/iodp.proc.350.104.2015>
- Thomson, D. J. (1982). Spectrum estimation and harmonic analysis. *Proceedings of the IEEE*, 70(9), 1055–1096. <https://doi.org/10.1109/PROC.1982.12433>
- Torrence, C., & Campo, G. P. (1998). A practical guide to wavelet analysis. *Bulletin of the American Meteorological Society*, 79(1), 61–78. [https://doi.org/10.1175/1520-0477\(1998\)079%3C0061:APGTWA%3E2.0.CO;2](https://doi.org/10.1175/1520-0477(1998)079%3C0061:APGTWA%3E2.0.CO;2)
- Venz, K. A., & Hodell, D. A. (2002). New evidence for changes in Plio–Pleistocene deep water circulation from Southern Ocean ODP leg 177 site 1090. *Palaeogeography, Palaeoclimatology, Palaeoecology*, 182(3–4), 197–220. [https://doi.org/10.1016/S0031-0182\(01\)00496-5](https://doi.org/10.1016/S0031-0182(01)00496-5)
- Venz, K. A., Hodell, D. A., Stanton, C., & Detlef, A. W. (1999). A 1.0 Myr record of glacial North Atlantic intermediate water variability from ODP site 982 in the northeast Atlantic. *Paleoceanography*, 14(1), 42–52. <https://doi.org/10.1029/1998PA000013>
- Verhelst, W. (2000). Overlap-add methods for time-scaling of speech. *Speech Communication*, 30(4), 207–221. [https://doi.org/10.1016/S0167-6393\(99\)00051-5](https://doi.org/10.1016/S0167-6393(99)00051-5)